Temperature effect on free vibration response of a smart multifunctional sandwich plate

Rasool Moradi-Dastjerdi and Kamran Behdinan

Temperature effect on free vibration response of a smart multifunctional sandwich plate

Journal:	*Journal of Sandwich Structures and Materials*
Manuscript ID	JSSM-19-0263.R1
Manuscript Type:	Standard Article
Date Submitted by the Author:	31-Oct-2019
Complete List of Authors:	Moradi-Dastjerdi, Rasool; University of Toronto - Mississauga, Department of Mechanical and Industrial Engineering Behdinan, Kamran; University of Toronto Department of Mechanical and Industrial Engineering
Keywords:	Natural frequencies, Thermal effect, Lightweight porous core, Graphene nanoparticle, Smart piezoceramic faces, Multifunctional sandwich plates
Abstract:	A smart multifunctional sandwich plate (SMSP) with a wide range of applications can be produced by proper arrangement of its layers. This paper offers an SMSP with one central lightweight porous layer, two middle polymer/graphene nanocomposite (PGNC) layers and two active faces made of a piezoceramic material. The coupled effects of temperature conditions and piezoelectric behavior on the natural frequencies of the proposed SMSP located on elastic foundations have been studied in the current research. For the dispersions of graphene particles and pores inside host layers, different functional profiles have been considered. Moreover, graphene particles and polymeric materials with temperature dependent material properties have been adopted. The mechanical properties of PGNC are evaluated by employing Halpin-Tsai approach which is modified to capture nanoscale effects. Eventually, the coupled governing eigenvalue equations of the proposed SMSP are derived using a third order theory called TSDT and are studied by a developed meshless solution. In addition, the effects of graphene, porosity, geometric and foundation aspects on the natural frequency of the proposed SMSP are studied. The results disclose that the natural frequencies of the proposed SMSPs are improved by embedding pores in core layer due to the remarkable reduction of structural weight. It is worth noting that nanocomposite layers can completely compensate the

1
2
3
4
5
6
7
8
9
10
11
12
13
14
15
16
17
18
19
20
21
22
23
24
25
26
27
28
29
30
31
32
33
34
35
36
37
38
39
40
41
42
43
44
45
46
47
48
49
50
51
52
53
54
55
56
57
58
59
60

| | structural stiffness reduction caused by embedding pores in the core. |
| | |

SCHOLARONE™
Manuscripts

Temperature effect on free vibration response of a smart multifunctional sandwich plate

Rasool Moradi-Dastjerdi[*] **and Kamran Behdinan**[†]

Advanced Research Laboratory for Multifunctional Lightweight Structures (ARL-MLS), Department of Mechanical & Industrial Engineering, University of Toronto, Toronto, Canada

Abstract

A smart multifunctional sandwich plate (SMSP) with a wide range of applications can be produced by proper arrangement of its layers. This paper offers an SMSP with one central lightweight porous layer, two middle polymer/graphene nanocomposite (PGNC) layers and two active faces made of a piezoceramic material. The coupled effects of temperature conditions and piezoelectric behavior on the natural frequencies of the proposed SMSP located on elastic foundations have been studied in the current research. For the dispersions of graphene particles and pores inside host layers, different functional profiles have been considered. Moreover, graphene particles and polymeric materials with temperature dependent material properties have been adopted. The mechanical properties of PGNC are evaluated by employing Halpin-Tsai approach which is modified to capture nanoscale effects. Eventually, the coupled governing eigenvalue equations of the proposed SMSP are derived using a third order theory called TSDT and are studied by a developed meshless solution. In addition, the effects of graphene, porosity, geometric and foundation aspects on the natural frequency of the proposed SMSP are studied. The results disclose that the natural frequencies of the proposed SMSPs are improved by embedding pores in core layer due to the remarkable reduction of structural weight. It is worth noting that nanocomposite layers can completely compensate the structural stiffness reduction caused by embedding pores in the core.

Keywords: Natural frequencies; Thermal effect; Lightweight porous core; Graphene nanoparticle; Smart piezoceramic faces; Multifunctional sandwich plates

---

[*] Email: moradi@mie.utoronto.ca

[†] Email: behdinan@mie.utoronto.ca

1

1. INTRODUCTION

Attaching piezoelectric patches on passive system structures can make structural responses applicable for self-controlling and self-monitoring smart systems. Depending on their passive structures and piezoelectric designs, these smart systems can also offer other engineering applications such as damping vibrations [1–3], energy harvesting [4], fluid delivery [5,6] and damage detection [7]. However, due to the brittle behavior of piezoelectric materials, they should be attached to softer passive structures which can be one of the main objectives in the design of such smart structures. Multifunctional sandwich structures with a softer core are appropriate candidates for the passive part of a smart structure due to their advantages. The enhancement of stiffness to weight ratio is one of the main concerns which results in the design of sandwich structure consisting of a lightweight core integrated with stiffer skins [8–10]. In this regard, polymeric materials carrying huge volumes of pores were recommended as lightweight materials with controllable thermomechanical properties [11]. In addition, polymers enhanced with nanoscale fillers such as graphene particles and carbon nanotubes (CNTs) are also recognized as lightweight nanocomposite materials [12–16]. Furthermore, utilizing functionally graded (FG) materials concept [17], the dispersions of nanofillers or pores in specified profiles can also intensify the benefits of nanocomposites and foams in sandwich structures [18,19].

Recently, mechanical and thermomechanical analyses of advanced multilayered structures have been become an interesting subject for researchers. For sandwich plates with layers made of homogeneous and FG materials, mechanical responses have been presented using refined plate theory (RPT) [20], modified higher order plate theory (HSDT) [21] and nth-order HSDT [22]. Moreover, modal [23] and stress [24] analyses of curved sandwich panels with FG layers were investigated using a HSDT based FEM. Utilizing Sanders shell theory, Qin et al. [25,26] presented free vibration responses of cylindrical shells. Duc and Cong [27] proposed auxetic cellular honeycomb plates with negative Poisson's ratio located between two aluminum faces and conducted vibrational analysis using first order plate theory (FSDT). The influence of thermal environment on the buckling loads and natural frequencies of viscoelastic plates integrated with FG ceramic/metal faces was investigated using FSDT [28]. For polymeric plates located between aggregated CNT/polymer faces, Sharif Zarei et al. [29] studied thermal and moist environment effects on natural frequency using HSDT. Considering the same structures, Safaei et al. [30,31] investigated thermal gradient influence on vibrational and stress wave responses using HSDT. Moradi-Dastjerdi et al. [32] considered a flexible lightweight plate

2

integrated with aggregated CNT/polymer faces and presented free vibration responses using FSDT and 3D elasticity for faces and flexible core, respectively. For multilayer PGNC structures, temperature influence on the nonlinear vibration responses of such multilayer plates was investigated using FSDT and a stress function [33]. Pashmforoush [34] conducted a statistical analysis on the vibrational response of PGNC plates. Furthermore, vibrational behaviors of plates [35,36], trapezoidal plates [37] and curved shells [38,39] made of PGNC were reported. Concerning porosity effect, natural frequencies of isotropic plates [40,41], PGNC cylindrical shells [42] and PGNC plates [43] were studied using FSDT. Zhao et al. [44] investigated the frequency responses of circular disks and rings with FG profiles of porosity dispersions using modified Fourier series and FSDT. Moreover, buckling loads and static responses of sandwich plates consisting of aggregated CNT/polymer faces and a polymeric core with uniform [45] and FG [46] profiles of pores were studied using HSDT based meshless solution.

Mechanical analysis of advanced structures with active piezoelectric fibers or layers is another interesting subject for researchers due to the extensive range of their potential applications. Askari Farsangi [47] provided a Levy solution based on FSDT to investigate the natural frequency of isotropic plates located between piezoceramic faces. Using a third order RPT, Rouzgar and Abad [48] developed an analytical solution to investigate the natural frequency of FG plates located between piezoceramics. For the same smart plates, Duc and Cong [49] studied nonlinear dynamic responses using TSDT based Galerkin method. Kpeky et al. [50] proposed two new elements and presented deflections and free vibration FEM analyses of isotropic beams, plates and shells with piezoceramic patches/faces. Arani et al. [51] designed a PD controller for CNT/polymer plates located between piezoelectric PVDF faces and studied the active natural frequency of proposed smart structures. Using FEM and FSDT, Tao et al. [4] conducted broadband energy harvesting study for bistable CNT/polymer plates located between piezoceramic faces. The vibrational responses of polymer/nanoclay plates located between piezoceramic faces were investigated using FSDT and a meshless solution by Moradi-Dastjerdi et al. [52]. Ghadiri and Hosseini [53] studied shock force and electrical input effects on the natural frequencies of nanoscale piezoceramic plates located between two graphene sheets. For FG piezoceramic plates with FG profiles of porosity dispersions, temperature influence was studied on natural frequencies using a four-variable RPT in [54]. The influence of porosity aspects on natural frequencies for porous plates located between piezoceramic faces were studied using Mindlin plate theory (MPT) and variational principle in [55]. The static and

3

vibrational deflections of FG PGNC plates with piezoceramic faces and FG profiles of porosity dispersions were presented using FEM and a C^0 type HSDT [56]. The natural frequency response of a five-layer curved shell consisting of a porous core, two middle CNT/polymer layers and two piezoelectric faces was performed by Setoodeh et al. [57].

This paper offers an SMSP with one central porous layer, two middle PGNC layers and two piezoceramic faces. Different functional profiles have been considered for the dispersions of graphene particles and pores inside their host layers. Moreover, temperature dependent material properties have been adopted for graphene particles and polymeric materials. The coupled effects of temperature conditions and piezoelectric behavior on the natural frequencies of SMSPs located on elastic foundations have been investigated using a TSDT based meshless solution. The mechanical properties of PGNC are evaluated by employing a modified Halpin-Tsai approach to capture nanoscale effects. The proposed SMSP has various potential engineering applications because it enjoys active piezoelectric effect, high strength to weight ratio, and comparatively manageable thermal response. Effects of graphene, porosity, geometric and foundation aspects on the natural frequency of the proposed SMSP are examined.

2. Modeling of SMSP

As illustrated in Fig. 1, SMSPs with one central lightweight porous layer and two middle PGNC layers integrated with two piezoceramic faces have been considered. SMSPs are located on elastic foundations with shear c_s and normal c_n coefficients and subjected to electrical input V_0 and thermal gradient effect such that the temperatures of upper and lower faces are T_u and T_d, respectively. In Fig. 1, the length, width and thickness of SMSPs are denoted by l_x, l_y and d, respectively. Moreover, the thickness of core, PGNC and piezoceramic layers are represented by d_c, d_n and d_p, respectively.

2.1. Porous core

Three profiles of void dispersions along the thickness of porous central layer, including uniform, symmetric (Sym.) and asymmetric (Asym.), have been considered. The mass density ρ^p, Poisson's ratio υ^p and elasticity modulus E^p of central porous layer are governed by

the volume (indicated by porosity parameters λ_0 and $\lambda_m = 1 - \sqrt{1 - \lambda_0}$) and profile dispersion

of voids. They can be estimated as follows [42,55]:

Uniform: $E^p = \left(\dfrac{2}{\pi} \sqrt{1 - \lambda_0} - \dfrac{2}{\pi} + 1 \right)^2 E^m$, $\rho^p = \left(\dfrac{2}{\pi} \sqrt{1 - \lambda_0} - \dfrac{2}{\pi} + 1 \right) \rho^m$ (1)

Sym.: $E^p(z) = \left(1 - \lambda_0 \cos\left(\dfrac{\pi z}{d_c} \right) \right) E^m$, $\rho^p(z) = \left(1 - \lambda_m \cos\left(\dfrac{\pi z}{d_c} \right) \right) \rho^m$ (2)

Asym.: $E^p(z) = \left(1 - \lambda_0 \cos\left(\dfrac{\pi z}{4 d_c} + \dfrac{\pi}{4} \right) \right) E^m$, $\rho^p(z) = \left(1 - \lambda_0 \cos\left(\dfrac{\pi z}{4 d_c} + \dfrac{\pi}{4} \right) \right) \rho^m$ (3)

All the profiles: $\upsilon^p(z) = 0.221\beta + \upsilon^m \left(0.342\beta^2 - 1.21\beta + 1 \right)$ (4)

where $\beta = 1 - \rho^p / \rho^m$ and superscript m denotes perfect (without any void) central layer. The

thermal expansion coefficient α^p and thermal conductivity C^p of porous core are evaluated

using the same utilized equations for E^p.
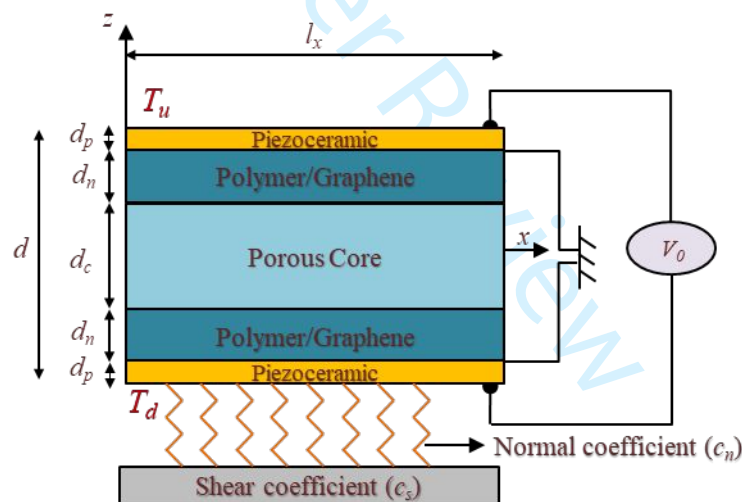
Fig 1. Layer arrangement of the proposed smart multifunctional sandwich plate

2.2. Nanocomposite layers

The dispersion profiles of randomly oriented graphene particles are also assumed to be

functional along the thickness of PGNC layers. These profiles of graphene volume fraction

$f_r(z)$ are governed by the exponent of graphene volume fraction m and their values at inner

f_{r-i} and outer f_{r-o} faces which are defined as follows:

5

Upper PGNC layer: $f_r(z) = f_{r-i} + \Delta f \left[1 + (2z - d_c - d_n)/2d_n \right]^m$ (5)

Lower PGNC layer: $f_r(z) = f_{r-i} + \Delta f \left[1 - (2z + d_c + d_n)/2d_n \right]^m$ (6)

where $\Delta f = f_{r-o} - f_{r-i}$.

Thermal conductivity of such PGNC layers C^n have been estimated considering the resistance of polymer/graphene interface R_k as follows [58,59]:

$$C^n(z) = C^m \frac{3 + f_r(z)\left[2\Gamma_1(1-L_1) + \Gamma_3(1-L_3) \right]}{3 - f_r(z)\left[2\Gamma_1 L_1 + \Gamma_3 L_3 \right]}$$ (7)

where

$$\Gamma_i = \frac{C_i - C^m}{C^m + L_i(C_i - C^m)} \quad , \quad i = 1, 3 \quad , \quad L_1 = \frac{q^2}{2(q^2-1)} - \frac{q}{2(q^2-1)^{3/2}} \cos^{-1} q \quad , \quad L_3 = 1 - 2L_1 \,,$$ (8)

$$C_i = \frac{C^g}{1 + \gamma_k \Gamma_i C^g / C^m}, \quad \gamma_k = (1 + 2q)C^m R_k / d^g \quad , \quad q = a^g / d^g$$

where the thickness, length and width of graphene particles are shown with d^g, a^g and b^g, respectively. In addition, the superscripts of n, g and m show PGNC, matrix and graphene, respectively.

Moreover, temperature dependent thermal expansion coefficient $\alpha^n(z,T)$ is estimated using the reported equation for composites reinforced with 3D randomly dispersed short fibers as follows [60]:

$$\alpha^n(z,T) = \frac{\left[E^n + 4\upsilon^n(1+\upsilon^n)K^n \right]\alpha_{11}^n + 4(1+\upsilon)K^n \alpha_{22}^n}{E^n + 4(1+\upsilon^n)^2 K^n}$$ (9)

where T is temperature, K^n is the effective bulk modulus of PGNC. The in-plane values of α_{11}^n and α_{22}^n are given below [61]:

$$\alpha_{11}^n(z,T) = \frac{f_r E_{11}^g \alpha_{11}^g + f_m E^m \alpha^m}{f_r E_{11}^g + f_m E^m}$$ (10)

$$\alpha_{22}^n(z,T) = (1+\upsilon^g) f_r \alpha_{22}^g + (1+\upsilon^m) f_m \alpha^m(T) - \upsilon^n \alpha_{11}^n(T)$$ (11)

in which the volume fraction of matrix material in PGNC is shown by $f_m = 1 - f_r$.

In the estimation of the elastic modulus of composites, Halpin-Tsai equations [62] usually provide comparatively accurate values due to considering the geometrical shapes of fillers. However, these equations should be modified for nanocomposite materials due to nanofiller/matrix interfaces and other size scale effects. In this regard, Shen et al. [61] imported

6

two efficiency parameters (s_1 and s_2) in original Halpin-Tsai equations to improve their accuracy in the estimation of E^n as shown below:

$$E^n(z,T) = \frac{3}{8}\left[s_1 \frac{1+2\left(a^g / d^g\right)\gamma_{11}^g f_r}{1-\gamma_{11}^g f_r} E^m \right] + \frac{5}{8}\left[s_2 \frac{1+2\left(b^g / d^g\right)\gamma_{22}^g f_r}{1-\gamma_{22}^g f_r} E^m \right] \tag{12}$$

where

$$\gamma_{11}^g = \frac{E_{11}^g / E^m - 1}{E_{11}^g / E^m + 2a^g / d^g} \quad , \quad \gamma_{22}^g = \frac{E_{22}^g / E^m - 1}{E_{22}^g / E^m + 2b^g / d^g} \tag{13}$$

2.3. Governing Equations

The prepared SMSPs are subjected to mechanical, thermal and piezoelectrical effects. The coupled governing equations for such advanced plates are defined as [5]:

$$\boldsymbol{\sigma} = \mathbf{Q}(\boldsymbol{\varepsilon} - \boldsymbol{\alpha}\Delta T) - \boldsymbol{\chi}^{\mathbf{T}}\mathbf{E}$$
$$\mathbf{D} = \boldsymbol{\chi}(\boldsymbol{\varepsilon} - \boldsymbol{\alpha}\Delta T) + \boldsymbol{\kappa}\mathbf{E} \tag{14}$$

where electrical displacement $\mathbf{D}$ and stress $\boldsymbol{\sigma}$ vectors are related to electrical field $\mathbf{E}$ and strain $\boldsymbol{\varepsilon}$ vectors using dielectric $\boldsymbol{\kappa}$, elastic stiffness $\mathbf{Q}$ and piezoelectric $\boldsymbol{\chi}$ constant matrices, and thermal expansion $\boldsymbol{\alpha}$ vector when temperature is changed as $\Delta T = T - T_0$ from room temperature $T_0 = 300K$. The definitions of these matrices and vectors are given below:

$$\boldsymbol{\sigma} = \left\{\boldsymbol{\sigma}_b \quad \boldsymbol{\sigma}_s\right\}^T, \boldsymbol{\sigma}_b = \left\{\sigma_{xx} \quad \sigma_{yy} \quad \tau_{xy}\right\}^T, \boldsymbol{\sigma}_s = \left\{\tau_{xz} \quad \tau_{yz}\right\}^T \tag{15}$$

$$\boldsymbol{\varepsilon} = \left\{\boldsymbol{\varepsilon}_b \quad \boldsymbol{\gamma}\right\}^T, \boldsymbol{\varepsilon}_b = \left\{\varepsilon_{xx} \quad \varepsilon_{yy} \quad \gamma_{xy}\right\}^T, \boldsymbol{\gamma} = \left\{\gamma_{yz} \quad \gamma_{xz}\right\}^T \tag{16}$$

$$\mathbf{E} = -\left\{0 \quad 0 \quad V_{,z}\right\}^T \tag{17}$$

$$\mathbf{Q} = \begin{bmatrix} \mathbf{Q}_b & 0 \\ 0 & \mathbf{Q}_s \end{bmatrix}, \mathbf{Q}_b = \begin{bmatrix} Q_{11} & Q_{12} & 0 \\ Q_{12} & Q_{22} & 0 \\ 0 & 0 & Q_{66} \end{bmatrix}, \mathbf{Q}_s = \begin{bmatrix} Q_{55} & 0 \\ 0 & Q_{44} \end{bmatrix} \tag{18}$$

$$\boldsymbol{\chi} = \begin{bmatrix} \boldsymbol{\chi}_b & \boldsymbol{\chi}_s \end{bmatrix}, \boldsymbol{\chi}_b = \begin{bmatrix} 0 & 0 & 0 \\ 0 & 0 & 0 \\ \chi_{31} & \chi_{32} & 0 \end{bmatrix}, \boldsymbol{\chi}_s = \begin{bmatrix} 0 & \chi_{15} \\ \chi_{24} & 0 \\ 0 & 0 \end{bmatrix} \tag{19}$$

$$\boldsymbol{\kappa} = \begin{bmatrix} \kappa_{11} & 0 & 0 \\ 0 & \kappa_{22} & 0 \\ 0 & 0 & \kappa_{33} \end{bmatrix} \tag{20}$$

7

where electric potential along the thickness of piezoelectric faces is shown by V.

The energy function Π of the proposed SMSP including strain energy, elastic foundation energy and kinematic energy can be written as [5,18]:

$$\Pi = \frac{1}{2}\int_{\Omega}\left[-\rho(z)(\dot{u}^2 + \dot{v}^2 + \dot{w}^2) + (\varepsilon - \alpha\Delta T)^T\sigma - E^T D\right]d\Omega + \frac{1}{2}\int_{A}\left[c_n w^2 + c_s\left[w_{,x}^2 + w_{,y}^2\right]\right]dA \tag{21}$$

where Ω and A are the volume and face area of SMSP, respectively. The in-plane (u and v) and out-of-plane w components of SMSP's deflections are determined as the following third order theory of plates [63]:

$$u = u_0 + z\eta_x + z^3\lambda_1\left(\eta_x + w_{0,x}\right)$$
$$v = v_0 + z\eta_y + z^3\lambda_1\left(\eta_y + w_{0,y}\right) \tag{22}$$
$$w = w_0$$

where $\lambda_1 = -4/3d^2$, mid-plane deflections are represented with subscript 0, and plate rotations are indicated by η_x and η_y. Using Eq. (22), the linear part of strain vectors are defined as below [63]:

$$\varepsilon_b = \varepsilon_0 + z\varepsilon_1 + \lambda_1 z^3\varepsilon_3 \quad , \quad \gamma = \left(1 + 3\lambda_1 z^2\right)\gamma_0 \tag{23}$$

where

$$\varepsilon_b = \left\{\begin{array}{c} u_{0,x} \\ v_{0,y} \\ u_{0,y} + v_{0,x} \end{array}\right\}, \varepsilon_1 = \left\{\begin{array}{c} \eta_{x,x} \\ \eta_{y,y} \\ \eta_{x,y} + \eta_{y,x} \end{array}\right\}, \varepsilon_3 = \left\{\begin{array}{c} \eta_{x,x} + w_{0,xx} \\ \eta_{y,y} + w_{0,yy} \\ \eta_{x,y} + \eta_{y,x} + 2w_{0,xy} \end{array}\right\}, \gamma_0 = \left\{\begin{array}{c} \eta_x + w_{0,x} \\ \eta_y + w_{0,y} \end{array}\right\} \tag{24}$$

3. Meshless Formulations

According to Eq. (22), the deflections of all nodes must have five unknowns (degree of freedoms, DOFs) including u_0, v_0, w_0, η_x and η_x. In this regard, a meshless solution with moving least squares (MLSs) shape functions are developed which approximate DOFs of displacement field **U** as follows [18]:

$$\hat{\mathbf{U}} = \left[\hat{u}_{0i}, \hat{v}_{0i}, \hat{w}_{0i}, \hat{\eta}_{xi}, \hat{\eta}_{yi} \right]^T = \sum_{i=1}^{n} N_i U_i \tag{25}$$

where shape functions and generalized DOF values for all nodes n in the domain are shown with N_i and $\hat{\mathbf{U}}$, respectively.

Using Eq. (25), the discretized definition of electric field (Eq. 17), displacement field (Eq. 22) and strain vectors (Eq. 23) are as follows:

$$\mathbf{E} = -\mathbf{\psi}_V \hat{\mathbf{V}} \tag{26}$$

$$\hat{\mathbf{u}} = \left\{ \hat{u}_i \quad \hat{v}_i \quad \hat{w}_i \right\}^T = \left\{ \mathbf{\varphi_0} + z\,\mathbf{\varphi}_1 + \lambda_1 z^3\,\mathbf{\varphi}_3 \right\} \hat{\mathbf{U}} \tag{27}$$

$$\mathbf{\varepsilon}_b = \left\{ \mathbf{\psi}_0 + z\,\mathbf{\psi}_1 + \lambda_1 z^3\,\mathbf{\psi}_3 \right\} \hat{\mathbf{U}} \quad , \quad \mathbf{\gamma} = \left(1 + 3\lambda_1 z^2 \right) \mathbf{\psi}_s\,\hat{\mathbf{U}} \tag{28}$$

where the definition of all $\mathbf{\psi}$ and $\mathbf{\varphi}$ matrices are given in Appendix. Introducing these equations and Eq. (14) into the equation of energy function (Eq. 21) and following the standard method, the governing Eigen value equation for the proposed SMSPs are determined as:

$$\mathbf{M}\ddot{\hat{\mathbf{U}}} + \left(\mathbf{K}_{uu} + \mathbf{K}_{ue}\mathbf{K}_{ee}^{-1}\mathbf{K}_{eu} \right) \hat{\mathbf{U}} = 0 \tag{29}$$

in which mass matrix $\mathbf{M}$ and stiffness matrices of mechanical $\mathbf{K}_{uu}$, coupling electro-mechanical $\mathbf{K}_{eu} = \mathbf{K}_{ue}^T$ and piezoelectric permittivity $\mathbf{K}_{ee}$ are determined as:

$$\mathbf{M} = \int_A \left[\mathbf{\varphi}_0^T \quad \mathbf{\varphi}_1^T \quad \mathbf{\varphi}_3^T \right] \overline{\mathbf{M}} \left[\mathbf{\varphi}_0 \quad \mathbf{\varphi}_1 \quad \mathbf{\varphi}_3 \right]^T dA \tag{30}$$

$$\begin{aligned}
\mathbf{K}_{uu} &= \int_A \left[\mathbf{\psi}_0^T \quad \mathbf{\psi}_1^T \quad \mathbf{\psi}_3^T \right] \overline{\mathbf{Q_b}} \left[\mathbf{\psi}_0 \quad \mathbf{\psi}_1 \quad \mathbf{\psi}_3 \right]^T dA \\
&+ \int_A \left[\mathbf{\psi}_s^T \quad \mathbf{\psi}_s^T \right] \overline{\mathbf{Q_s}} \left[\mathbf{\psi}_s \quad \mathbf{\psi}_s \right]^T dA + \int_A \left(\mathbf{\varphi}_n^T c_n \mathbf{\varphi}_n + \mathbf{\varphi}_s^T c_s \mathbf{\varphi}_s \right) dA
\end{aligned} \tag{31}$$

$$\mathbf{K}_{ue} = \int_A \left[\mathbf{\psi}_0^T \quad \mathbf{\psi}_1^T \quad \mathbf{\psi}_3^T \right] \overline{\mathbf{\chi}_{be}} \mathbf{\psi}_v dA + \int_A \left[\mathbf{\psi}_s^T \quad \mathbf{\psi}_s^T \right] \overline{\mathbf{\chi}_{se}} \mathbf{\psi}_v dA \tag{32}$$

$$\mathbf{K}_{ee} = \int_A \mathbf{\psi}_v^T \overline{\mathbf{\kappa}} \mathbf{\psi}_v\, dA \tag{33}$$

where:

9

$$\overline{\mathbf{M}} = \int_{-h/2}^{h/2} \rho \begin{bmatrix} 1 & z & \lambda_1 z^3 \\ & z^2 & \lambda_1 z^4 \\ Sym. & & \lambda_1^2 z^6 \end{bmatrix} dz \quad , \quad \overline{\mathbf{\kappa}} = \int_{-h/2}^{h/2} \mathbf{\kappa} \, dz \tag{34}$$

$$\overline{\mathbf{\chi}_{be}} = \int_{-h/2}^{h/2} \{1 \quad z \quad \lambda_1 z^3\}^T \mathbf{\chi}_b \, dz \quad , \quad \overline{\mathbf{\chi}_{se}} = \int_{-h/2}^{h/2} \{1 \quad 3\lambda_1 z^2\}^T \mathbf{\chi}_s \, dz \tag{35}$$

$$\overline{\mathbf{Q_b}} = \int_{-h/2}^{h/2} \begin{bmatrix} 1 & z & \lambda_1 z^3 \\ & z^2 & \lambda_1 z^4 \\ Sym. & & \lambda_1^2 z^6 \end{bmatrix} \mathbf{Q}_b dz \quad , \quad \overline{\mathbf{Q_s}} = \int_{-h/2}^{h/2} \begin{bmatrix} 1 & 3\lambda_1 z^2 \\ 3\lambda_1 z^2 & 9\lambda_1^2 z^4 \end{bmatrix} \mathbf{Q}_s dz \tag{36}$$

$\mathbf{\varphi}_n$ and $\mathbf{\varphi}_s$ are defined in Appendix.

4. Results and discussions

Here, first, the developed meshless solution was validated. Then, steady state heat conduction behavior and free vibration of the proposed SMSPs were investigated. PZT-4 piezoceramic, PMMA/graphene and neat PMMA are adopted as the materials of outer piezoelectric, middle nanocomposite and (porous) core layers, respectively. The following temperature dependent E and α are utilized for PMMA and graphene particles (with $a^g = 14.76$ nm, $b^g = 14.77$ nm and $d^g = 0.188$ nm) [61]:

$$E_{11}^g = (2.16637 - 0.00193T + 2.93701 \times 10^{-6} T^2 - 1.51775 \times 10^{-9} T^3) \text{ TPa}$$
$$E_{22}^g = (2.16868 - 0.00193T + 2.85954 \times 10^{-6} T^2 - 1.45145 \times 10^{-9} T^3) \text{ TPa} \tag{37}$$
$$E^m = (3.52 - 0.0034T) GPa$$

$$\alpha_{11}^g = (-3.83788 - 0.01416T - 1.63355 \times 10^{-5} T^2 + 6.33589 \times 10^{-9} T^3) \times 10^{-6} / K$$
$$\alpha_{22}^g = (-3.73997 - 0.01296T - 1.35033 \times 10^{-5} T^2 + 4.60392 \times 10^{-9} T^3) \times 10^{-6} / K \tag{38}$$
$$\alpha^m = 45(1 + 0.0005\Delta T) \times 10^{-6} / K$$

The constant properties of the utilized materials are also considered as follows:

PZT-4 [64]: $\chi_{31} = \chi_{32} = -5.2 \, C/m^2$, $\chi_{51} = \chi_{24} = 12.7 \, C/m^2$, $\kappa_{11} = \kappa_{22} = 13 \times 10^{-9} \, F/m$,

$\kappa_{33} = 11.5 \times 10^{-9} \, F/m$, $Q_{11}^p = 81.3 \, GPa$, $Q_{55}^p = 25.6 \, GPa$, $\rho^p = 7500 \, kg/m^3$, $C^p = 2.1 \, W/mK$,

$\alpha^p = 2\left(10^{-6} / K\right)$

PMMA: $\upsilon^m = 0.34$, $\rho^m = 1150 \, kg/m^3$, $C^m = 0.247 \, W/mK$ [61]

10

Graphene: $\upsilon^g = 0.177$, $\rho^g = 4118\,kg/m^3$ [61], $C^g = 5000\,W/mK$ [65],

$R_k = 3\times10^{-9}\,K.m^2/W$ [66]

Shen et al. [61] determined the values of efficiency parameters (s_1 and s_2) defined in Eq. (12)for some particular nanofiller volume fractions at three temperatures, as shown in Table 1. Therefore, their direct application in nanocomposites with smooth variation of f_r or under temperature gradient effect does not provide accurate results. Hence, a 2D spline interpolation with respect to f_r and T is implemented on s_1 and s_2 to generate a smooth approximation on s_1 and s_2 in $300 < T\,(K) < 500$ and $3 < f_r\,(\%) < 11$ [67].

Furthermore, for the constants of foundation, the normalized forms of $C_s = c_s a^2/D^m$ and

$C_n = c_n a^2/D^m$ are utilized $D^m = E^m d^3/12\left(1-\left(\upsilon^m\right)^2\right)$.

Table 1 The utilized graphene efficiency parameters [61]

T (K)	f_r (%)	3	5	7	9	11
300	s_1	2.929	3.068	3.013	2.647	2.311
	s_2	2.855	2.962	2.966	2.609	2.260
400	s_1	2.977	3.128	3.060	2.701	2.405
	s_2	2.896	3.023	3.027	2.603	2.337
500	s_1	3.388	3.544	3.462	3.058	2.736
	s_2	3.382	3.414	3.339	2.936	2.665

4.1. Validation study

Due to the lack of experimental or even numerical results for the proposed SMSP in literatures, the accuracy of the provided solution is examined by comparing the first-five natural frequencies obtained for a Ti-6Al-4V plate located between piezoelectric G-1195N faces with available data. For this smart plate, the dimensions are $l_x=l_y=400$ mm, $d_c=5$ mm and $d_p=0.1$ mm. Considering the same material properties, present FSDT and TSDT based meshless results are compared with the results obtained from classical laminated plate theory (CLPT) [68], MPT [55], FSDT [47] and a third order RPT [48], as summarized in Table 2. The comparison reveals a good accuracy for the provided method particularly when the results are compared with those presented in [48] which employed higher order plate theory.

11

Convergence study is also presented in this subsection for the proposed SMSP with clamped edges, $l_x = l_y = 1$ m, $d_c = 20$ mm, $d_n = 2$ mm, $d_p = 0.5$ mm, and without elastic foundation ($C_n = C_s = 0$). Noted, these details are utilized for all following simulations unless otherwise mentioned. Figure 2 shows the fundamental frequency of the proposed SMSP at room temperature versus the distributed nodal arrangement of $n \times n$ when f_r is linearly varied from 3% to 11% through PGNC thickness, and porosity dispersion with $\lambda_0 = 0.8$ is symmetrically varied through core thickness. Good convergence for the developed meshless solution is observed in this figure such that the frequency does not change after $n = 17$ which has been adopted for all following models.

Table 2 The first frequencies (Hz) of a Ti-6Al-4V plate located between G-1195N faces

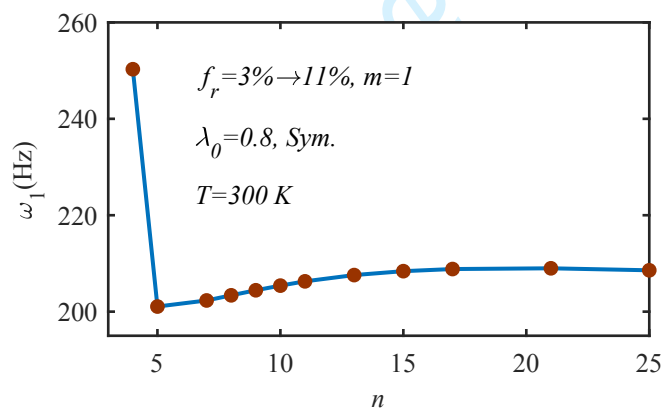| Theory	1st	2nd	3rd	4th	5th
CLPT [68]	144.25	359.00	359.00	564.10	717.80
MPT [55]	144.94	362.01	362.01	578.69	722.92
FSDT [47]	145.35	363.05	363.05	580.35	725.00
3rd order RPT [48]	145.35	363.06	363.06	580.37	725.03
Present (FSDT)	146.55	366.00	366.00	585.86	730.97
Present (TSDT)	146.18	363.39	363.55	579.07	718.94

Fig. 2. Fundamental frequency ω_1 of SMSP versus the node arrangement of $n \times n$

4.2. Steady state thermal response

The influences of porosity and graphene contents on the temperature responses of SMSPs with $d_n = 8$ mm and $d_p = 2$ mm subjected to $T_d = 300$ and $T_u = 400$ K are illustrated in Fig. 3. Figure 3a illustrates that the dispersion or volume of porosity can significantly affect not only the

temperature profiles of core layer but also those of nanocomposite layers. <mark>It should be mentioned that the temperature profile of a layer is governed by the thermal conductivities of that layer. The embedded pores in core act as a thermal barrier. Therefore, due to the significant effect of porosity dispersion on the thermal conductivity of core layer, it considerably affects the temperature profile of SMSP, especially in core layer which is the thickest layer.</mark> As expected, SMSPs with perfect or uniform porous central layers have linear temperature profiles. Figure 3b discloses that lower values of m improve the thermal conductivity of PGNC layer due to the increase of graphene content in PGNC layers.
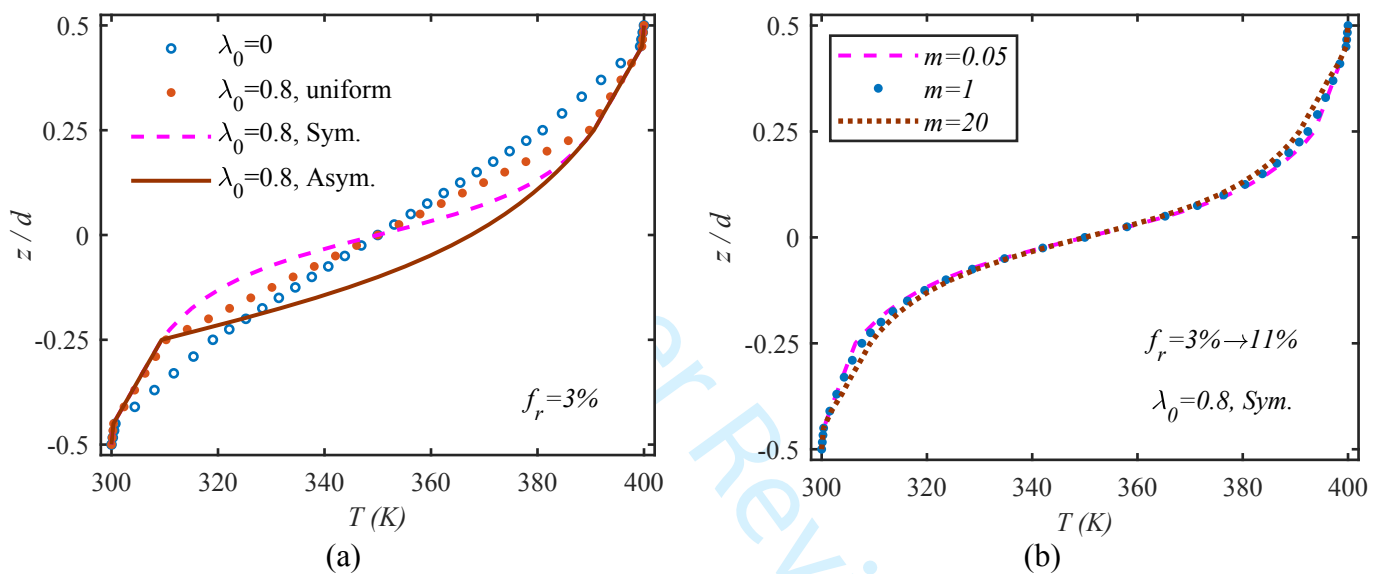

Fig. 3 The influences of (a) porosity and (b) graphene contents on the resulted temperature profiles of SMSPs

4.3. Natural frequency response

The influences of all aspects of the proposed SMSP on the fundamental natural frequency are studied in this subsection. First, fundamental natural frequencies are plotted versus temperature at upper surface for different graphene dispersions m and volumes of pores λ_0 when $T_d = 300$ K, as can be seen in Figs. 4a and 4b. By reducing structural stiffness, the increase of temperature gradient reduces ω in all cases. Because of decreasing graphene content, higher values of m introduce fewer natural frequencies, as shown in Fig. 4a. Interestingly, the increase of porosity volume increases the frequency of SMSP due to structural weight reduction.
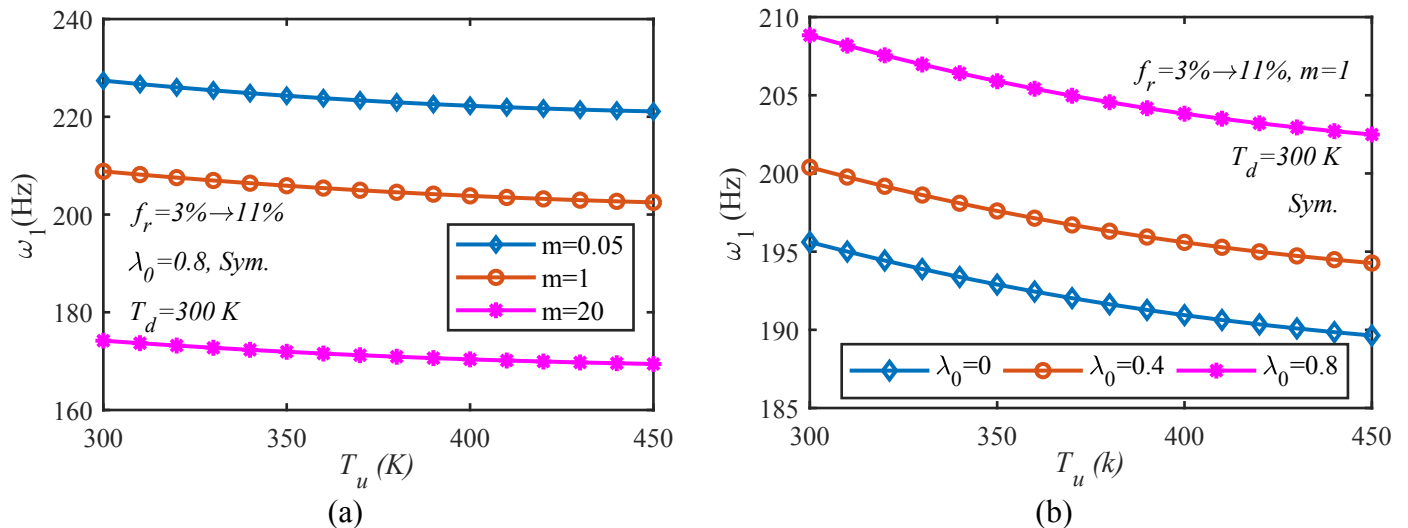
13

(a)

(b)

Fig. 4 Fundamental frequency of SMSP versus temperature at upper face for different (a) graphene dispersions (b) pores volumes

The influences of graphene aspects on the frequencies of the proposed SMSP are illustrated in Fig. 5 for different values of m and λ_0 when temperature is changed from 300 K at lower face to 400 K at upper one and graphene volume fraction is varied from $f_{r\text{-}i}$=3 % at the inner faces of PGNC to different values of $f_{r\text{-}o}$ at their outer faces. Regardless of the variation of other parameters, the increase of $f_{r\text{-}o}$ generally improves SMSP frequencies due to the better enhancement of the stiffness of PGNC. This effect is more noticeable in graphene dispersion profiles with lower m values, as shown in Fig 5a. However, Fig. 5b reveals that the frequencies of SMSP with porous or perfect central layers are enhanced by increasing $f_{r\text{-}o}$ in the same trend.
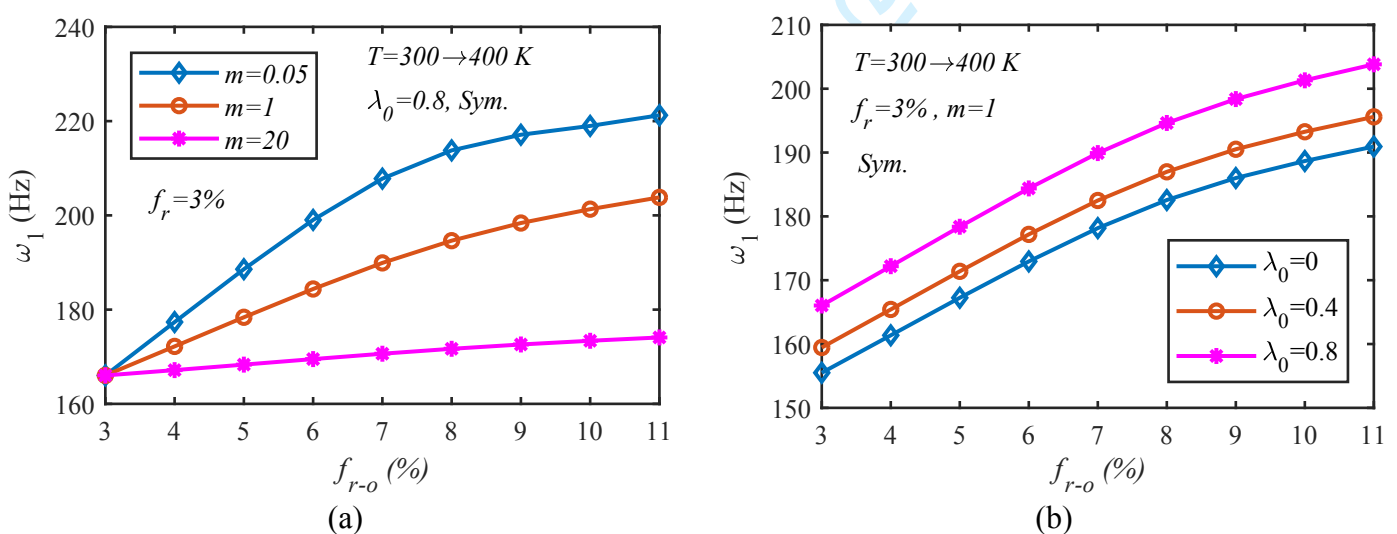

(a)

(b)

Fig. 5 Fundamental frequency of SMSP versus graphene volume at outer faces for different (a) graphene dispersions (b) pores volumes

14

Porosity influence on the natural frequency of SMSPs with linear variation of graphene content from $f_{r-i} = 3\%$ to $f_{r-o} = 11\%$ are plotted in Fig. 6. It is observed that embedding more pores inside central layer improves the natural frequencies of SMSP due to remarkable reduction of structural weight. It is worth noting that nanocomposite layers can completely compensate the stiffness reduction caused by pores inside the core. Fig. 6a shows that porosity dispersion profile has an insignificant effect on the natural frequencies of SMSP, although it can completely change steady state temperature profile as shown in Fig. 3a. The reason is the stiffness of PGNC and piezoceramic layers are much higher than the stiffness of porous core layer which is the nearest layer to the neutral axis of SMSP. In addition, all the three profiles of porosity dispersion have the same porosity volume fraction. Therefore, porosity dispersion cannot remarkably affect the structural stiffness to weight ratio, and consequently, it has an insignificant effect on the natural frequency of SMSP. Moreover, the natural frequency of SMSP is decreased by raising environmental temperature as illustrated in Fig. 6b due to the decreases of the elastic moduli of PMMA and graphene particles according to Eq. (37).

(a)   (b)
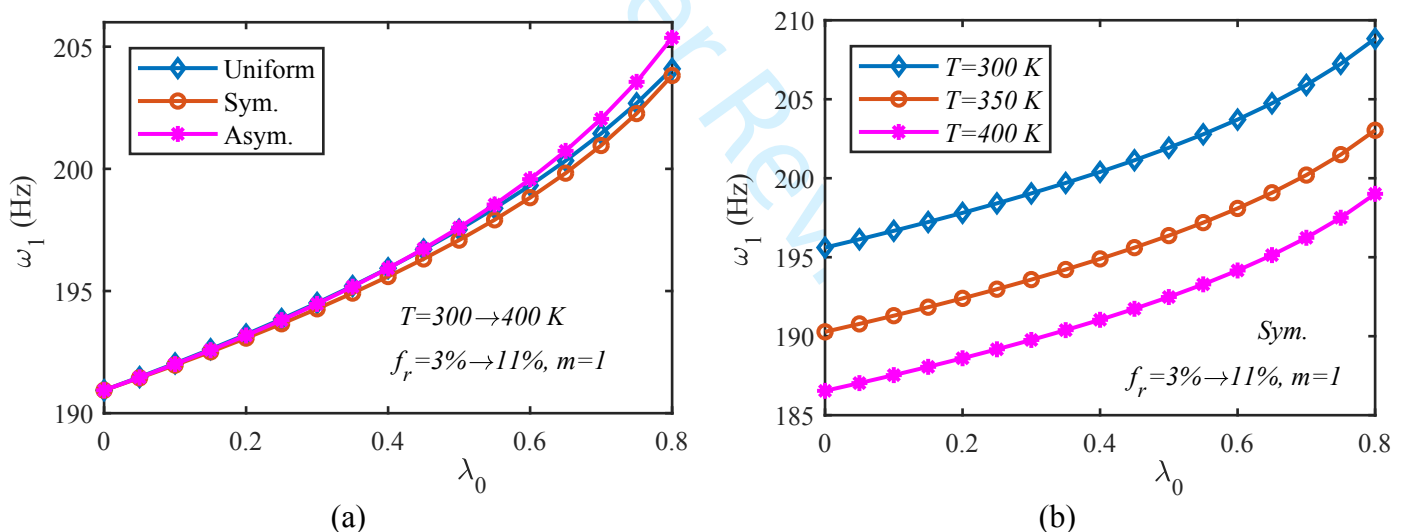
Fig. 6 Fundamental frequency of SMSP versus porosity volume for different (a) porosity dispersions (b) environment temperatures

Core thickness influence on the natural frequency of the proposed SMSPs with symmetric porous central layer at $T_d = 300$ K and $T_u = 400$ K is illustrated in Figs. 7a and 7b for $f_r = 3\%$ and $f_r = 11\%$, respectively. The increase of core thickness generally improves the natural frequency of SMSP such that sharp increases in ω are observed when d_c is increased up to about 30 mm. In these cases, embedding more porosity results in SMSPs with higher natural

15

frequencies. However, there are specific core thicknesses at both graphene volume fractions that introduce SMSPs with natural frequency independent from porosity volume. It means that, embedding pores has no effects on the natural frequency of such structures.
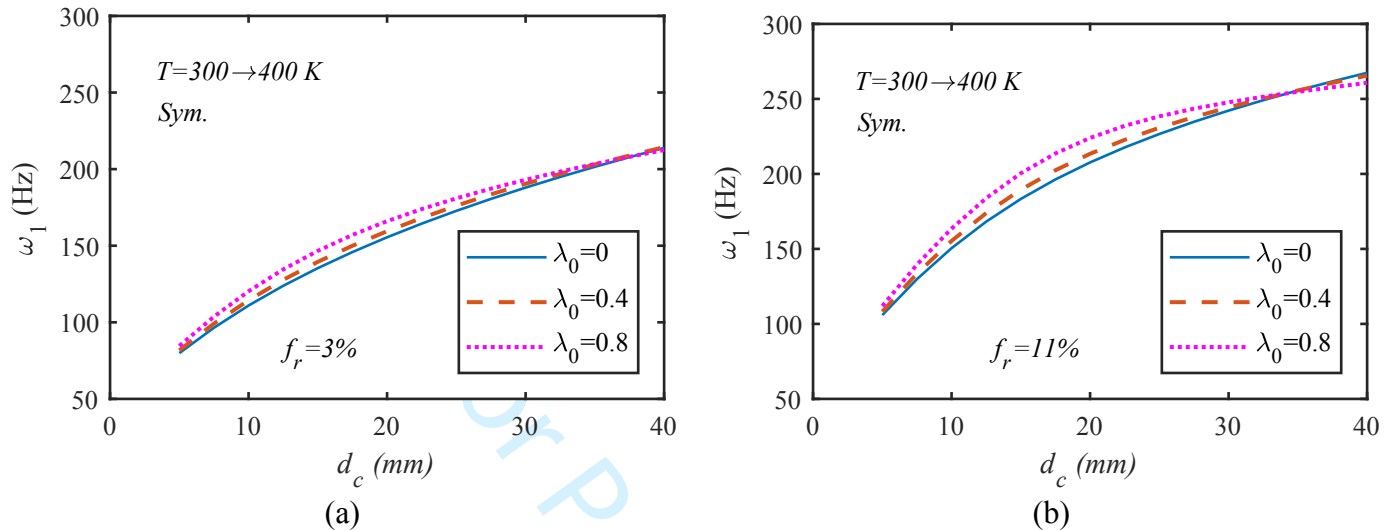

(a)　　　　　　　　　　　　　　　　　(b)

Fig. 7 Fundamental frequencies of SMSPs versus core thickness when (a) f_r = 3% and (b) f_r = 11%

The relation between PGNC thickness and the natural frequency of SMSPs with perfect and porous cores is illustrated in Fig. 8 for f_{r-i} = 3%, f_{r-o} = 11%, T_d = 300 K, and T_u = 400 K. Due to the presence of higher graphene content, PGNCs with lower m values introduce SMSPs with higher natural frequencies. It is also found that the use of thicker PGNC layers provides SMSPs with higher natural frequencies. Comparing Fig. 8 with Fig. 7 reveals that increasing the thickness of middle layers of nanocomposite has much stronger impact on natural frequencies of SMSPs than increasing the thickness of central layer. The reasons can be their distances from neural axis and huge differences between their elastic moduli.
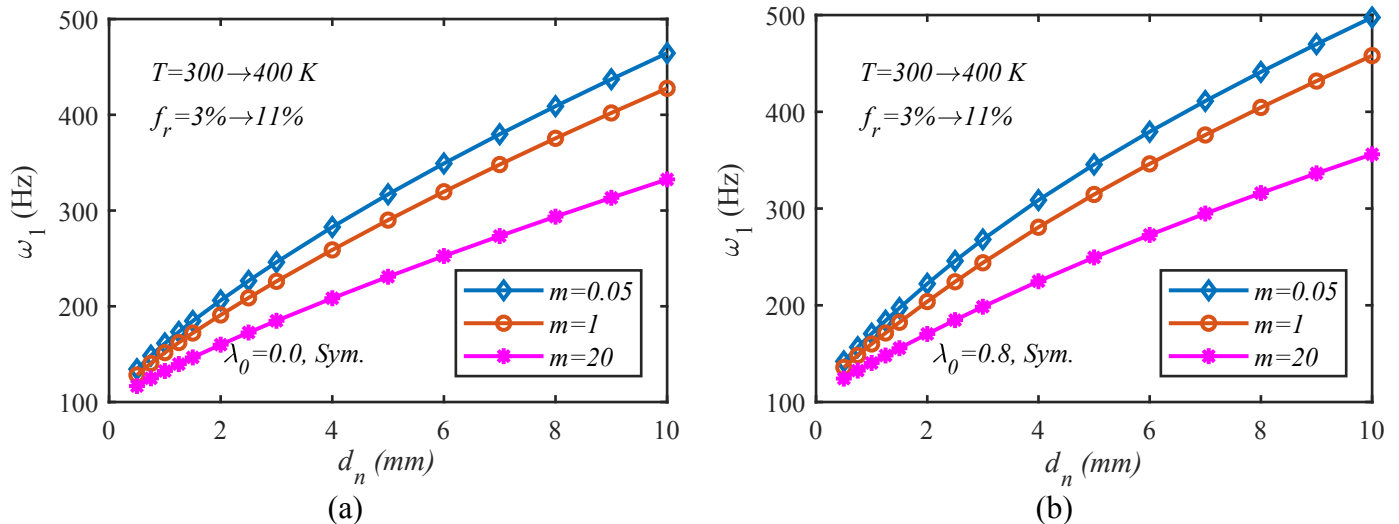
16

(a)

(b)

Fig. 8 Fundamental frequencies of SMSPs versus PGNC layer thickness when (a) $\lambda_0 = 0$ and

(b) $\lambda_0 = 0.8$

The influence of piezoceramic thickness on the natural frequency of SMSPs with symmetric porous core, $\lambda_0 = 0.8$, $T_d = 300$ K and $T_u = 400$ K are illustrated in Fig. 9 for different uniform dispersed graphene contents. In SMSPs with $f_r = 3\%$, the improvement of natural frequency is observed when piezoceramic thickness is increased. However, at higher values of f_r, the use of thicker piezoceramic layers does not increase the natural frequencies of SMSPs. The reason is that the elasticity modulus of PGNC layers with high f_r are higher than those of piezoceramic layers.
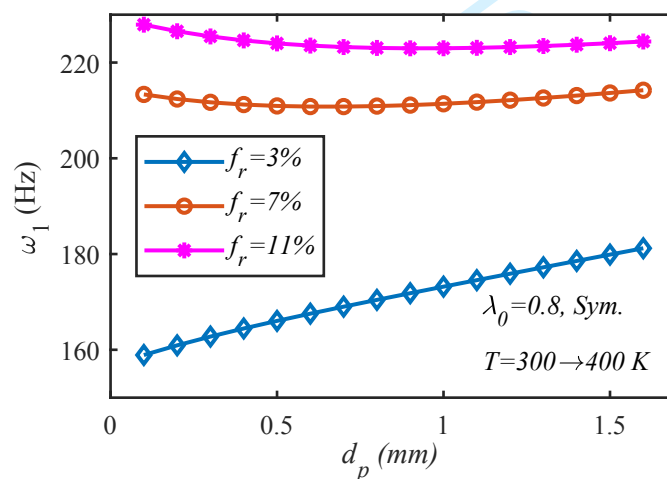

Fig. 9 Fundamental frequency of SMSPs versus piezoceramic thickness

Table 3 presents the natural frequency of different types of SMSPs under various thermal conditions for two electrical boundary conditions of open-circuit (OC) and close-circuit (CC).

17

The schematic loop of the utilized OC electrical boundary condition is illustrated in Fig. 1. For CC electrical boundary condition, both faces of piezoceramic layers are grounded; therefore, SMSP is turned to a passive structure. Table 3 shows that the natural frequencies of active (OC) SMSPs are a little higher than passive (CC) ones due to piezoelectric effect. Moreover, the natural frequencies of SMSPs under thermal gradient effects of $T_d = 300$ K and $T_u = 400$ K are higher than those at the thermal environment of $T = 350$ K.

Table 4 presents the effects of the aspect ratio (l_y/l_x) of SMSP foundation coefficients (C_n and C_s) and edge constrain type on the natural frequencies of SMSPs with symmetric porous cores, $\lambda_0 = 0.8$, $f_{r-i} = 3\%$, $f_{r-o} = 11\%$, $m = 1$, $T_d = 300$ K, and $T_u = 400$ K. The increase of the aspect ratio of SMSP from $l_y/l_x = 1$ to $l_y/l_x = 2$ dramatically reduces natural frequency; however, further increases of l_y/l_x has an insignificant effect on the natural frequency of SMSP. Furthermore, the frequencies of SMSPs located on elastic foundations are higher than those of SMSPs without foundation such that C_s has more effects than C_n. Finally, the decrease of frequency is observed when edges lose the number of their constrains such that among the studied boundary conditions, fully clamped and fully simply supported SMSPs have the highest and lowest natural frequencies, respectively.

Table 3. Fundamental frequencies of SMSPs ω_1(Hz) with perfect and symmetric porous cores

T (K)	λ_0	Circuit	$d_p = 0.1$ mm			$d_p = 0.5$ mm		
			$f_r = 3\%$	$f_r = 7\%$	$f_r = 11\%$	$f_r = 3\%$	$f_r = 7\%$	$f_r = 11\%$
300	0	OC	148.45	199.96	213.09	158.82	200.60	212.06
		CC	148.27	199.84	212.99	158.13	200.11	211.61
	0.8	OC	163.43	219.33	233.39	169.66	216.01	228.68
		CC	163.25	219.22	233.29	168.99	215.52	228.23
350	0	OC	143.65	193.85	207.23	154.96	195.34	206.95
		CC	143.46	193.73	207.12	154.26	194.84	206.49
	0.8	OC	158.11	212.60	226.97	165.39	210.27	223.14
		CC	157.92	212.49	226.87	164.70	209.77	222.69
400	0	OC	140.59	189.35	203.26	152.42	191.46	203.51
		CC	140.39	189.23	203.15	151.71	190.95	203.05
	0.8	OC	154.67	207.67	222.68	162.56	206.09	219.50
		CC	154.48	207.55	222.57	161.87	205.59	219.04
300→400	0	OC	144.33	194.46	208.02	155.50	195.89	207.66
		CC	144.15	194.35	207.92	154.80	195.38	207.20
	0.8	OC	158.91	213.34	227.92	166.03	210.94	224.00
		CC	158.72	213.23	227.81	165.35	210.44	223.54

Table 4. Fundamental frequencies of SMSPs ω_I(Hz) with symmetric porous cores, λ_0=0.8, f_{r-i} = 3%, f_{r-o} = 11%, m = 1, T_d = 300 K, and T_u = 400 K (C: clamped edge, S: simply supported edge)

B.C.	C_n	C_s	l_y/l_x=1	l_y/l_x=2	l_y/l_x=4	l_y/l_x=8
CCCC	0	0	203.82	142.87	132.32	130.34
	200	0	205.46	145.19	134.83	132.88
	0	20	207.23	145.96	135.16	133.10
CSCS	0	0	171.70	89.99	71.70	67.88
	200	0	173.63	93.63	76.22	72.64
	0	20	175.61	94.54	76.45	72.65
SSSS	0	0	131.95	83.25	70.90	67.80
	200	0	134.46	87.18	75.47	72.56
	0	20	136.86	88.07	75.68	72.57

5. Conclusions

A multifunctional smart sandwich plate was proposed by layer arrangement of two piezoceramic faces, two middle FG polymer/graphene layers and one central FG porous in this paper. The coupled effects of temperature conditions and piezoelectric behavior on the natural frequencies of SMSPs located on elastic foundations were studied using a TSDT based meshless solution. It was observed that porosity aspects significantly affect the temperature profiles of core and nanocomposite layers. Moreover, embedding porosity in core layer increases the natural frequency of SMSPs due to the remarkable reduction of structural weight. However, some specific core thicknesses were captured such that embedding porosity does not affect the natural frequency of SMSP. Regarding the effect of graphene aspects, the results disclosed that the increase of graphene content generally improves natural frequency. This effect can be intensified or relieved by changing graphene distribution profile or the thickness of piezoceramic layers, respectively. Finally, a reduction in the natural frequency of SMSP was observed by increasing the temperature of environment or thermal gradient effect because of the reduction of structural stiffness.

Acknowledgements

Appendix

$$\boldsymbol{\psi}_v = \begin{bmatrix} 0 & 0 & 1/d_p \end{bmatrix} \tag{A1}$$

$$\boldsymbol{\psi}_0 = \begin{bmatrix} N_{i,x} & 0 & 0 & 0 & 0 \\ 0 & N_{i,y} & 0 & 0 & 0 \\ N_{i,y} & N_{i,x} & 0 & 0 & 0 \end{bmatrix}, \boldsymbol{\psi}_1 = \begin{bmatrix} 0 & 0 & 0 & N_{i,x} & 0 \\ 0 & 0 & 0 & 0 & N_{i,y} \\ 0 & 0 & 0 & N_{i,y} & N_{i,x} \end{bmatrix},$$

$$\boldsymbol{\psi}_3 = \begin{bmatrix} 0 & 0 & N_{i,xx} & N_{i,x} & 0 \\ 0 & 0 & N_{i,yy} & 0 & N_{i,y} \\ 0 & 0 & 2N_{i,xy} & N_{i,y} & N_{i,x} \end{bmatrix}, \boldsymbol{\psi}_s = \begin{bmatrix} 0 & 0 & N_{i,x} & N_i & 0 \\ 0 & 0 & N_{i,y} & 0 & N_i \end{bmatrix} \tag{A2}$$

$$\boldsymbol{\varphi}_n = \begin{bmatrix} 0 & 0 & N_i & 0 & 0 \end{bmatrix}, \boldsymbol{\varphi}_s = \begin{bmatrix} 0 & 0 & N_{i,x} & 0 & 0 \\ 0 & 0 & N_{i,y} & 0 & 0 \end{bmatrix} \tag{A3}$$

$$\boldsymbol{\varphi}_0 = \begin{bmatrix} N_i & 0 & 0 & 0 & 0 \\ 0 & N_i & 0 & 0 & 0 \\ 0 & 0 & N_i & 0 & 0 \end{bmatrix}, \boldsymbol{\varphi}_1 = \begin{bmatrix} 0 & 0 & 0 & N_i & 0 \\ 0 & 0 & 0 & 0 & N_i \\ 0 & 0 & 0 & 0 & 0 \end{bmatrix}, \boldsymbol{\varphi}_3 = \begin{bmatrix} 0 & 0 & N_{i,x} & N_i & 0 \\ 0 & 0 & N_{i,y} & 0 & N_i \\ 0 & 0 & 0 & 0 & 0 \end{bmatrix} \tag{A4}$$

References

[1]　Kundalwal SI, Kumar RS, Ray MC. Smart damping of laminated fuzzy fiber reinforced composite shells using 1-3 piezoelectric composites. Smart Mater Struct 2013;22:10500. doi:10.1177/1077546314543726.

[2]　Kundalwal SI, Ray MC. Smart damping of fuzzy fiber reinforced composite plates using 1-3 piezoelectric composites. J Vib Control 2016;22:1526–1546. doi:10.1177/1077546314543726.

[3]　Kamarian S, Bodaghi M, Pourasghar A, Talebi S. Vibrational behavior of non-uniform piezoelectric sandwich beams made of CNT-reinforced polymer nanocomposite by considering the agglomeration effect of CNTs. Polym Compos 2017;38:E553–62. doi:10.1002/pc.23933.

[4]　Tao J, He X, Yi S, Deng Y. Broadband energy harvesting by using bistable FG-CNTRC plate with integrated piezoelectric layers. Smart Mater Struct 2019;28:095021. doi:10.1088/1361-665X/ab2dc2.

[5]　Moradi-Dastjerdi R, Meguid SA, Rashahmadi S. Dynamic behavior of novel micro fuel pump using zinc oxide nanocomposite diaphragm. Sensors Actuators A Phys 2019;297:111528. doi:10.1016/j.sna.2019.111528.

[6]　Moradi-Dastjerdi R, Meguid SA, Rashahmadi S. Dynamic behavior of novel nanocomposite diaphragm in piezoelectrically-actuated micropump. Smart Mater Struct 2019;28:105022.

doi:10.1088/1361-665X/ab39c0.

[7]   Kapuria S, Kumari P. Boundary layer effects in Levy-type rectangular piezoelectric composite plates using a coupled efficient layerwise theory. Eur J Mech A/Solids 2012;36:122–40. doi:10.1016/j.euromechsol.2012.02.015.

[8]   Vinson JR. Sandwich Structures. Appl Mech Rev 2001;54:201. doi:10.1115/1.3097295.

[9]   Sobhani Aragh B, Yas MH. Effect of continuously grading fiber orientation face sheets on vibration of sandwich panels with FGM core. Int J Mech Sci 2011;53:628–38. doi:10.1016/J.IJMECSCI.2011.05.009.

[10]   Shokri-Oojghaz R, Moradi-Dastjerdi R, Mohammadi H, Behdinan K. Stress distributions in nanocomposite sandwich cylinders reinforced by aggregated carbon nanotube. Polym Compos 2019;40:E1918–27. doi:10.1002/pc.25206.

[11]   Aram E, Mehdipour-Ataei S. A review on the micro- and nanoporous polymeric foams : Preparation and properties. Int J Polym Mater Polym Biomater 2016;65:358–75. doi:10.1080/00914037.2015.1129948.

[12]   Pourasghar A, Chen Z. Nonlinear vibration and modal analysis of FG nanocomposite sandwich beams reinforced by aggregated CNTs. Polym Eng Sci 2019. doi:10.1002/pen.25119.

[13]   Qin Z, Pang X, Safaei B, Chu F. Free vibration analysis of rotating functionally graded CNT reinforced composite cylindrical shells with arbitrary boundary conditions. Compos Struct 2019;220:847–60. doi:10.1016/j.compstruct.2019.04.046.

[14]   Safaei B, Naseradinmousavi P, Rahmani A. Development of an accurate molecular mechanics model for buckling behavior of multi-walled carbon nanotubes under axial compression. J Mol Graph Model 2016;65:43–60. doi:10.1016/j.jmgm.2016.02.001.

[15]   Iacobellis V, Radhi A, Behdinan K. A bridging cell multiscale modeling of carbon nanotube-reinforced aluminum nanocomposites. Compos Struct 2018;202:406–12. doi:10.1016/j.compstruct.2018.02.044.

[16]   Qin Z, Safaei B, Pang X, Chu F. Traveling wave analysis of rotating functionally graded graphene platelet reinforced nanocomposite cylindrical shells with general boundary conditions. Results Phys 2019:102752. doi:10.1016/j.rinp.2019.102752.

[17]   Sahmani S, Safaei B. Nonlocal strain gradient nonlinear resonance of bi-directional functionally graded composite micro/nano-beams under periodic soft excitation. Thin-Walled Struct 2019;143:106226. doi:10.1016/J.TWS.2019.106226.

[18]   Moradi-Dastjerdi R, Aghadavoudi F. Static analysis of functionally graded nanocomposite sandwich plates reinforced by defected CNT. Compos Struct 2018;200:839–48. doi:10.1016/j.compstruct.2018.05.122.

[19]   Moradi-dastjerdi R, Behdinan K. Stability analysis of multifunctional smart sandwich plates with graphene nanocomposite and porous layers. Int J Mech Sci 2019:105283. doi:10.1016/j.ijmecsci.2019.105283.

21

[20]   Meziane MAA, Abdelaziz HH, Tounsi A. An efficient and simple refined theory for buckling and free vibration of exponentially graded sandwich plates under various boundary conditions. J Sandw Struct Mater 2014;16:293–318. doi:10.1177/1099636214526852.

[21]   Meksi R, Benyoucef S, Mahmoudi A, Tounsi A, Abbas E, Bedia A, et al. An analytical solution for bending, buckling and vibration responses of FGM sandwich plates. J Sandw Struct Mater 2019;21:727–57. doi:10.1177/1099636217698443.

[22]   Fu T, Chen Z, Yu H, Wang Z, Liu X. Free vibration of functionally graded sandwich plates based on nth-order shear deformation theory via differential quadrature method. J Sandw Struct Mater 2018. doi:10.1177/1099636218809451.

[23]   Dash S, Mehar K, Sharma N, Mahapatra TR, Panda SK. Modal analysis of FG sandwich doubly curved shell structure. Struct Eng Mech 2018;68:721. doi:10.12989/SEM.2018.68.6.721.

[24]   Dash S, Mehar K, Sharma N, Mahapatra TR, Panda SK. Finite element solution of stress and flexural strength of functionally graded doubly curved sandwich shell panel. Earthquakes Struct 2019;16:55. doi:10.12989/EAS.2019.16.1.055.

[25]   Qin Z, Yang Z, Zu J, Chu F. Free vibration analysis of rotating cylindrical shells coupled with moderately thick annular plates. Int J Mech Sci 2018;142–143:127–39. doi:10.1016/j.ijmecsci.2018.04.044.

[26]   Qin Z, Chu F, Zu J. Free vibrations of cylindrical shells with arbitrary boundary conditions : A comparison study. Int J Mech Sci 2017;133:91–9. doi:10.1016/j.ijmecsci.2017.08.012.

[27]   Duc ND, Cong PH. Nonlinear dynamic response and vibration of sandwich composite plates with negative Poisson's ratio in auxetic honeycombs. J Sandw Struct Mater 2018;20:692–717. doi:10.1177/1099636216674729.

[28]   Joseph S V, Mohanty SC. Temperature effects on buckling and vibration characteristics of sandwich plate with viscoelastic core and functionally graded material constraining layer. J Sandw Struct Mater 2019;21:1557–77. doi:10.1177/1099636217722309.

[29]   Sharif Zarei M, Hajmohammad MH, Mostafavifar M, Mohammadimehr M. Influence of temperature change and humidity condition on free vibration analysis of a nano composite sandwich plate resting on orthotropic Pasternak foundation by considering agglomeration effect. J Sandw Struct Mater 2017. doi:10.1177/1099636217735118.

[30]   Safaei B, Moradi-Dastjerdi R, Qin Z, Behdinan K, Chu F. Determination of thermoelastic stress wave propagation in nanocomposite sandwich plates reinforced by clusters of carbon nanotubes. J Sandw Struct Mater 2019:DOI: 10.1177/109963621984828. doi:10.1177/1099636219848282.

[31]   Safaei B, Moradi-Dastjerdi R, Qin Z, Chu F. Frequency-dependent forced vibration analysis of nanocomposite sandwich plate under thermo-mechanical loads. Compos Part B Eng 2019;161:44–54. doi:10.1016/j.compositesb.2018.10.049.

22

[32] Moradi-Dastjerdi R, Malek-Mohammadi H, Momeni-Khabisi H. Free vibration analysis of nanocomposite sandwich plates reinforced with CNT aggregates. ZAMM - J Appl Math Mech / Zeitschrift Fur Angew Math Und Mech 2017;97:1418–35. doi:10.1002/zamm.201600209.

[33] Cong HP, Duc ND. New approach to investigate the nonlinear dynamic response and vibration of a functionally graded multilayer graphene nanocomposite plate on a viscoelastic Pasternak medium in a thermal environment. Acta Mech 2018;229:3651–70. doi:10.1007/s00707-018-2178-3.

[34] Pashmforoush F. Statistical analysis on free vibration behavior of functionally graded nanocomposite plates reinforced by graphene platelets. Compos Struct 2019;213:14–24. doi:10.1016/J.COMPSTRUCT.2019.01.066.

[35] Fan Y, Xiang Y, Shen H-S. Nonlinear forced vibration of FG-GRC laminated plates resting on visco-Pasternak foundations. Compos Struct 2019;209:443–52. doi:10.1016/j.compstruct.2018.10.084.

[36] Kiani Y. Isogeometric large amplitude free vibration of graphene reinforced laminated plates in thermal environment using NURBS formulation. Comput Methods Appl Mech Eng 2018;332:86–101. doi:10.1016/J.CMA.2017.12.015.

[37] Zhao Z, Feng C, Wang Y, Yang J. Bending and vibration analysis of functionally graded trapezoidal nanocomposite plates reinforced with graphene nanoplatelets (GPLs). Compos Struct 2017;180:799–808. doi:10.1016/J.COMPSTRUCT.2017.08.044.

[38] Wang A, Chen H, Hao Y, Zhang W. Vibration and bending behavior of functionally graded nanocomposite doubly-curved shallow shells reinforced by graphene nanoplatelets. Results Phys 2018;9:550–9. doi:10.1016/J.RINP.2018.02.062.

[39] Fazelzadeh SA, Rahmani S, Ghavanloo E, Marzocca P. Journal of Thermal Stresses Thermoelastic vibration of doubly-curved nano-composite shells reinforced by graphene nanoplatelets. J Therm Stress 2019;42:1–17. doi:10.1080/01495739.2018.1524733.

[40] Thang PT, Nguyen-Thoi T, Lee D, Kang J, Lee J. Elastic buckling and free vibration analyses of porous-cellular plates with uniform and non-uniform porosity distributions. Aerosp Sci Technol 2018;79:278–87. doi:10.1016/j.ast.2018.06.010.

[41] Xue Y, Jin G, Ma X, Chen H, Ye T, Chen M, et al. Free vibration analysis of porous plates with porosity distributions in the thickness and in-plane directions using isogeometric approach. Int J Mech Sci 2019;152:346–62. doi:10.1016/j.ijmecsci.2019.01.004.

[42] Barati MR, Zenkour AM. Vibration analysis of functionally graded graphene platelet reinforced cylindrical shells with different porosity distributions. Mech Adv Mater Struct 2018. doi:10.1080/15376494.2018.1444235.

[43] Yang J, Chen D, Kitipornchai S. Buckling and free vibration analyses of functionally graded graphene reinforced porous nanocomposite plates based on Chebyshev-Ritz method. Compos Struct 2018;193:281–94. doi:10.1016/J.COMPSTRUCT.2018.03.090.

23

[44]   Zhao J, Xie F, Wang A, Shuai C, Tang J, Wang Q. Dynamics analysis of functionally graded porous (FGP) circular , annular and sector plates with general elastic restraints. Compos Part B 2019;159:20–43. doi:10.1016/j.compositesb.2018.08.114.

[45]   Safaei B, Moradi-Dastjerdi R, Behdinan K, Chu F. Critical buckling temperature and force in porous sandwich plates with CNT-reinforced nanocomposite layers. Aerosp Sci Technol 2019;91:175–85. doi:10.1016/j.ast.2019.05.020.

[46]   Safaei B, Moradi-Dastjerdi R, Behdinan K, Qin Z, Chu F. Thermoelastic behavior of sandwich plates with porous polymeric core and CNT clusters/polymer nanocomposite layers. Compos Struct 2019;226:111209. doi:10.1016/J.COMPSTRUCT.2019.111209.

[47]   Askari Farsangi MA, Saidi AR, Batra RC. Analytical solution for free vibrations of moderately thick hybrid piezoelectric laminated plates. J Sound Vib 2013;332:5981–5998. doi:10.1016/j.jsv.2013.05.010.

[48]   Rouzegar J, Abad F. Free vibration analysis of FG plate with piezoelectric layers using four-variable refined plate theory. Thin-Walled Struct 2015;89:76–83. doi:10.1016/J.TWS.2014.12.010.

[49]   Duc DN, Cong HP. Nonlinear thermo-mechanical dynamic analysis and vibration of higher order shear deformable piezoelectric functionally graded material sandwich plates resting on elastic foundations. J Sandw Struct Mater 2018;20:191–218. doi:10.1177/1099636216648488.

[50]   Kpeky F, Abed-Meraim F, Boudaoud H, Mostafa Daya E. Linear and quadratic solid-shell finite elements SHB8PSE and SHB20E for the modeling of piezoelectric sandwich structures Linear and quadratic solid-shell finite elements SHB8PSE and SHB20E for the modeling of piezoelectric sandwich structures. Mech Adv Mater Struct 2018;25:559–78. doi:10.1080/15376494.2017.1285466.

[51]   Arani AG, Jafari GS, Kolahchi R. Vibration analysis of nanocomposite microplates integrated with sensor and actuator layers using surface SSDPT. Polym Compos 2018;39:1936–49. doi:10.1002/pc.24150.

[52]   Moradi-Dastjerdi R, Meguid SA, Rashahmadi S. Electro-dynamic analysis of smart nanoclay-reinforced plates with integrated piezoelectric layers. Appl Math Model 2019;75:267–78. doi:10.1016/j.apm.2019.05.033.

[53]   Ghadiri M, Hosseini SH. Nonlinear forced vibration of graphene/ piezoelectric sandwich nanoplates subjected to a mechanical shock. J Sandw Struct Mater 2019:DOI: 10.1177/1099636219849647. doi:10.1177/1099636219849647.

[54]   Barati MR, Zenkour AM. Electro-thermoelastic vibration of plates made of porous functionally graded piezoelectric materials under various boundary conditions. J Vib Control 2018;24:1910–26. doi:10.1177/1077546316672788.

[55]   Askari M, Saidi AR, Rezaei AS. An investigation over the effect of piezoelectricity and porosity distribution on natural frequencies of porous smart plates. J Sandw Struct Mater 2018.

doi:10.1177/1099636218791092.

[56]   Nguyen LB, Nguyen N V, Thai CH, Ferreira AMJ, Nguyen-xuan H. An isogeometric Bézier
       finite element analysis for piezoelectric FG porous plates reinforced by graphene platelets.
       Compos Struct 2019;214:227–45. doi:10.1016/j.compstruct.2019.01.077.

[57]   Setoodeh AR, Shojaee M, Malekzadeh P. Vibrational behavior of doubly curved smart
       sandwich shells with FG-CNTRC face sheets and FG porous core. Compos Part B Eng
       2019;165:798–822. doi:10.1016/J.COMPOSITESB.2019.01.022.

[58]   Shen X, Wang Z, Wu Y, Liu X, He YB, Kim JK. Multilayer Graphene Enables Higher
       Efficiency in Improving Thermal Conductivities of Graphene/Epoxy Composites. Nano Lett
       2016;16:3585–93. doi:10.1021/acs.nanolett.6b00722.

[59]   Li M, Zhou H, Zhang Y, Liao Y, Zhou H. Effect of defects on thermal conductivity of
       graphene/epoxy nanocomposites. Carbon N Y 2018;130:295–303.
       doi:10.1016/j.carbon.2017.12.110.

[60]   Craft WJ, Christensen RM. Coefficient of Thermal Expansion for Composites with Randomly
       Oriented Fibers. J Compos Mater 1981;15:2–20. doi:10.1177/002199838101500102.

[61]   Shen HS, Lin F, Xiang Y. Nonlinear bending and thermal postbuckling of functionally graded
       graphene-reinforced composite laminated beams resting on elastic foundations. Eng Struct
       2017;140:89–97.

[62]   Halpin JC, Kardos JL. The Halpin-Tsai equations: a review. Polym Eng Sci 1976;16:344–52.

[63]   Reddy JN. Mechanics of laminated composite plates and shells: theory and analysis. CRC
       press; 2004.

[64]   Komeili A, Akbarzadeh AH, Doroushi A, Eslami MR. Static Analysis of Functionally Graded
       Piezoelectric Beams under Thermo-Electro-Mechanical Loads. Adv Mech Eng 2011;2011:1–
       10. doi:10.1155/2011/153731.

[65]   Balandin AA, Ghosh S, Bao W, Calizo I, Teweldebrhan D, Miao F, et al. Superior Thermal
       Conductivity of Single-Layer Graphene. Nano Lett 2008;8:902–7.

[66]   Konatham D, Striolo A. Thermal boundary resistance at the graphene-oil interface. Appl Phys
       Lett 2009;95:163105. doi:10.1063/1.3251794.

[67]   Moradi-Dastjerdi R, Behdinan K. Thermoelastic static and vibrational behaviors of
       nanocomposite thick cylinders reinforced with graphene. Steel Compos Struct 2019;31:529–39.
       doi:https://doi.org/10.12989/scs.2019.31.5.529.

[68]   He XQ, Ng TY, Sivashanker S, Liew KM. Active control of FGM plates with integrated
       piezoelectric sensors and actuators. Int J Solids Struct 2001;38:1641–55.